# EXPERIMENTAL INVESTIGATION OF FLUID-PARTICLE INTERACTION IN BINDER JET 3D PRINTING

Joshua J. Wagner*, Hang Shu*, Rahul Kilambi*, and C. Fred Higgs III*

*Department of Mechanical Engineering, Rice University, Houston, TX 77005

## ABSTRACT

Wide-scale adoption of binder jet 3D printing for mission-critical components in aerospace, biomedical, defense, and energy applications requires improvement in mechanical properties and performance characteristics of end-use components. Increased fidelity may be achieved with better understanding of the interfacial physics and complex fluid-particle interactions fundamental to the process. In this work, an experimental testing apparatus and procedure is developed to investigate the fluid and particle dynamics occurring upon impact of jetted binder droplets onto a powder bed. High-speed, microscopic imaging is employed to capture short time-scale phenomena such as ballistic particle ejection, capillary flow, and particle clustering. The effects of different process parameters (e.g., translational printhead velocity, jetting frequency, and impact velocity) on the dynamics of Inconel powder are studied. These experiments reveal that the fluid-particle interaction is significantly affected by a combination of printing parameters, ultimately governing the quality and performance of binder jet 3D printed components.

## 1. INTRODUCTION

Binder jet 3D printing (BJ3DP) is a type of powder bed additive manufacturing (AM) process that utilizes a scanning printhead to selectively administer fluid binder into a powder layer to form a cross-section of a three-dimensional object. The process is carried out in a series of repetitive cycles, each one producing an additional cross-section on top of the previous such that the components are built up layer-by-layer [1]. The major stages of the BJ3DP procedure are shown in Fig. 1. A single-layer print cycle begins with a powder delivery stage (Fig. 1a) where the feedstock material is forced to flow from a hopper onto the previously deposited layer. A counter-rotating roller then traverses the build area spreading the newly supplied powder into a thin layer (Fig. 1b). Next, a printhead dispenses binder from a multitude of inkjet nozzles into the layer to join particles in regions prescribed by a computer-aided design (CAD) model (Fig. 1c). After jetting, the build platform lowers by a specified layer thickness (Fig. 1d), and the process repeats until the components are fully constructed. After completion, the components are buried in unbound powder (Fig. 1e); therefore, a depowdering step is required for retrieval. Typically, the printed parts are then either sintered or infiltrated with a secondary material in a high-temperature furnace for densification and strengthening [2]. An extensive review of BJ3DP, from its development to present state-of-the-art, is given in [3].

The underlying physics of the BJ3DP process allows for many unique advantages compared to other AM methods, such as a wide range of suitable materials, relatively fast build times, and cost-effectiveness. These advantages have generated interest in BJ3DP for many applications in a variety of industrial sectors; however, its end-use components generally have

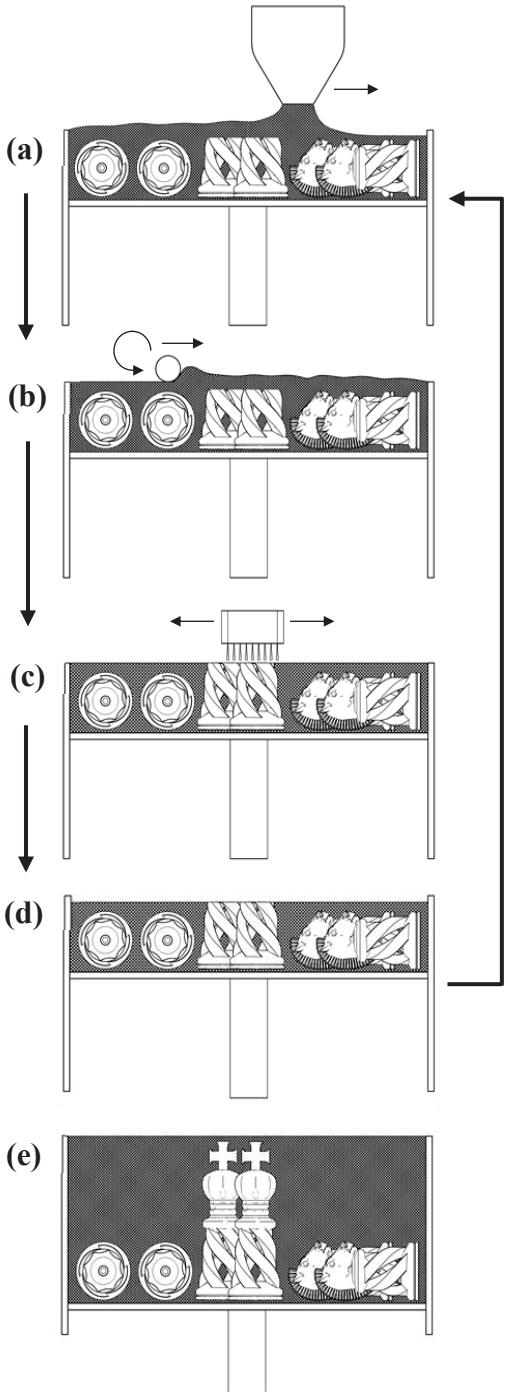


**FIGURE 1.** The general BJ3DP process comprised of the following stages: (a) powder delivery, (b) powder spreading, (c) binder jetting, and (d) build platform lowering. The stages (a)-(b) are repeated until the complete geometries are formed (e). Note that hatched regions indicate unbound powder.

increased porosity and less robust mechanical properties compared to powder bed fusion type AM processes. These downfalls have limited the use of BJ3DP for the fabrication of high-performance parts in demanding applications [4], e.g., combustion chambers for liquid rocket engines [5] or pressure vessel components in nuclear fusion reactors [6]. Therefore, mitigating these issues is of vital importance to facilitate a more wide-spread implementation of BJ3DP among a range of industries.

To achieve this, many research efforts have been carried out in each major stage of the process. Several powder dispensing (Fig. 1a) techniques have been explored for use in powder bed AM methods – a review of which is given in [7]. Powder spreading (Fig. 1b) simulations were performed using discrete element modeling (DEM) to better understand how spreading parameters affect the quality of the layer [8, 9]. The binder jetting stage (Fig. 1c) has been studied by a number of researchers; several of the important works on this topic are presented in the following section. Finally, there have been efforts to improve the various post-processing techniques often used to strengthen binder jetted parts, e.g., see [10, 11, 12].

The goal of this work is to develop an experimental apparatus and testing procedure that allows for investigation of the interfacial fluid-particle interaction prevalent during the binder jetting stage. Ultimately, this platform will provide insight on how printing parameters can be tuned to achieve optimal printing characteristics for a particular feedstock powder. The apparatus is constructed to replicate the fundamental printing operations in such a way that allows for quantative measurements of the print quality depending on various input parameter combinations. High-speed, microscopic imaging is employed to capture short time-scale dynamics occurring upon the impact of jetted binder droplets onto a powder bed. A dimensional analysis of the process reveals pertinent dimensionless groups that influence the coupled fluid and particle dynamics. Experiments are carried out to determine the effects

that certain dimensionless groups have on powder binding behavior.

## 2. FLUID-PARTICLE INTERACTION IN BJ3DP

The instant a jetted binder droplet impinges the powder bed, many physical phenomena begin to take place that govern the formation of bound particle features that make up the part. Immediately upon impact, momentum transferred from the droplet to the unconsolidated powder bed can result in ballistic ejection of particles. This potentially gives rise to various types of part defects; for example, the ejection of particles yield impact craters which are deleterious to dimensional accuracy and serve to increase porosity [13].

At impact, inertial forces initially drive the flow of liquid either into or on top of the bed. As the initial kinetic energy of the drop is transferred and dissipated into the powder bed, the binder may continue to flow into the interstitial space between particles due to capillary forces [14]. Simultaneously, the liquid attempts to minimize its surface energy by generating interfacial forces which impede the expansion of surface area as the binder spreads. These interfacial effects, namely surface tension and capillary action, often produce a net attractive force between mutually wetted particles. If these forces are large enough to overcome particle inertia and friction, the particles can be accelerated and drawn inward towards each other, forming a bound cluster referred to as a "primitive" [15].

A single-drop primitive is the most basic building element produced in BJ3DP. The printhead translates over the powder bed at a given velocity where, ideally, successive droplets coalesce with the previous ones forming a single-line primitive [16]. The line primitives must then be adequately stitched to adjacent lines to form a solid cross-section of the part. Additionally, the liquid should penetrate the powder bed deep enough to achieve sufficient inter-layer binding. For these reasons, the formation of line primitives is a predominant factor governing the relative density, dimensional accuracy, resolution, surface properties, and overall quality of the parts.

In Ref. [29], high-speed imaging of the fluid-particle interaction in BJ3DP was performed with synchrotron X-rays using the Advanced Photon Source at Argonne National Laboratory. With this approach, an X-ray beam passes completely through the powder bed and is converted to visible light on the opposite side. This approach has provided new insights into the surface and sub-surface dynamics of the powder bed during binder jetting. At the powder bed surface, ballistic ejection, impact cratering, and primitive formation were observed for several powder types of varying particle size and morphology. Powder bed compression induced by the droplet impact was discovered, and the depth of disturbance for each powder was reported. Although this work has offered knowledge about the effect of particle size and shape on the binder-powder interactions, the influence of printing parameters on primitive formation remains poorly understood. These parameters are commonly wrapped into a single expression [17] given as

$$S = \frac{\pi D_b^3}{6\Delta x \Delta y \Delta z (1-\phi)}\,, \tag{1}$$

where $D_b$ is the binder droplet diameter, $\Delta x$ is the droplet spacing, $\Delta y$ is the line spacing, $\Delta z$ is the layer thickness, and $\phi$ is the powder bed packing fraction. The droplet spacing is determined from the translational dispenser velocity, $U_d$, and the jetting frequency, $f_j$, by

$$\Delta x = \frac{U_d}{f_j} \ . \tag{2}$$

The binder saturation, $S$, given in Eq. (1) expresses the ratio of binder volume to void volume in a predefined envelope ($\Delta x \times \Delta y \times \Delta z$) within the powder bed. Saturation is an important parameter that must be optimized for particular feedstocks. Typically, higher saturation results in increased green (pre-sintered) part strength; however, excessive binder will bleed out of the desired part boundaries reducing dimensional accuracy and resolution [14]. Presently, the optimal saturation for a given powder is most often found by trial and error; however, several efforts have been made to obtain it more rigorously. In Ref. [18], an analytical model was developed to estimate the saturation level that results in a balance of capillary pressure dependent on contact angle of the solid-liquid-gas interface, binder-air surface tension, and powder bed packing fraction. This "equilibrium saturation" was first suggested to be the optimal saturation for BJ3DP in Ref. [14] based on arguments from the classical theory of fluid flow in porous media [19]. A more direct experimental approach was taken in Ref. [20] by analyzing the influence of saturation on the dimensional accuracy and surface roughness of 420 stainless steel parts. The same methodology was adopted in Ref. [21] to investigate how saturation affects the flexural strength of 316L stainless steel parts. Further studies regarding the appropriate selection of saturation level for various powders were carried out in Refs. [22, 23, 24, 25].

While some success in improving part quality was achieved in the above works, saturation alone is not sufficient to fully characterize the effects of fluid-particle interaction in BJ3DP. This is primarily due to the fact that saturation is not a unique value, which is made clear by closer inspection of Eq. (1). An infinite combination of the variables on the right-hand side may produce the same saturation value; however, holding saturation constant while changing other parameters does not guarantee that primitive formation behavior will remain the same. For example, a reduction of binder droplet diameter, $D_b$, can be accompanied with a thinner layer thickness, $\Delta z$, to produce the same value of $S$, but a decreased $D_b$ will also reduce the kinetic energy of the jetted droplet, which can dramatically change the impact dynamics. In this work, a dimensional analysis is performed to reveal how important parameters are related and how they should be varied in order to carry out valid parametric studies (Sec. 3).

## 3. EXPERIMENTAL SETUP

A testing apparatus was constructed to allow for close investigation of fluid-particle interaction in BJ3DP and the effect printing parameters have on the binding of a single-line primitive. The apparatus (Fig. 2) is comprised of a linear motor that drives a single-jet droplet dispenser over a powder sample at an adjustable translation speed, $U_d$, along an x-axis rail. The x-axis motor and rail assembly is mounted on a linear stage that allows for precise manual adjustment of the dispenser's y-axis position. The dispenser device, manufactured by MicroFab Technologies, Inc., utilizes a piezoelectric element for droplet generation, which provides control of jetting

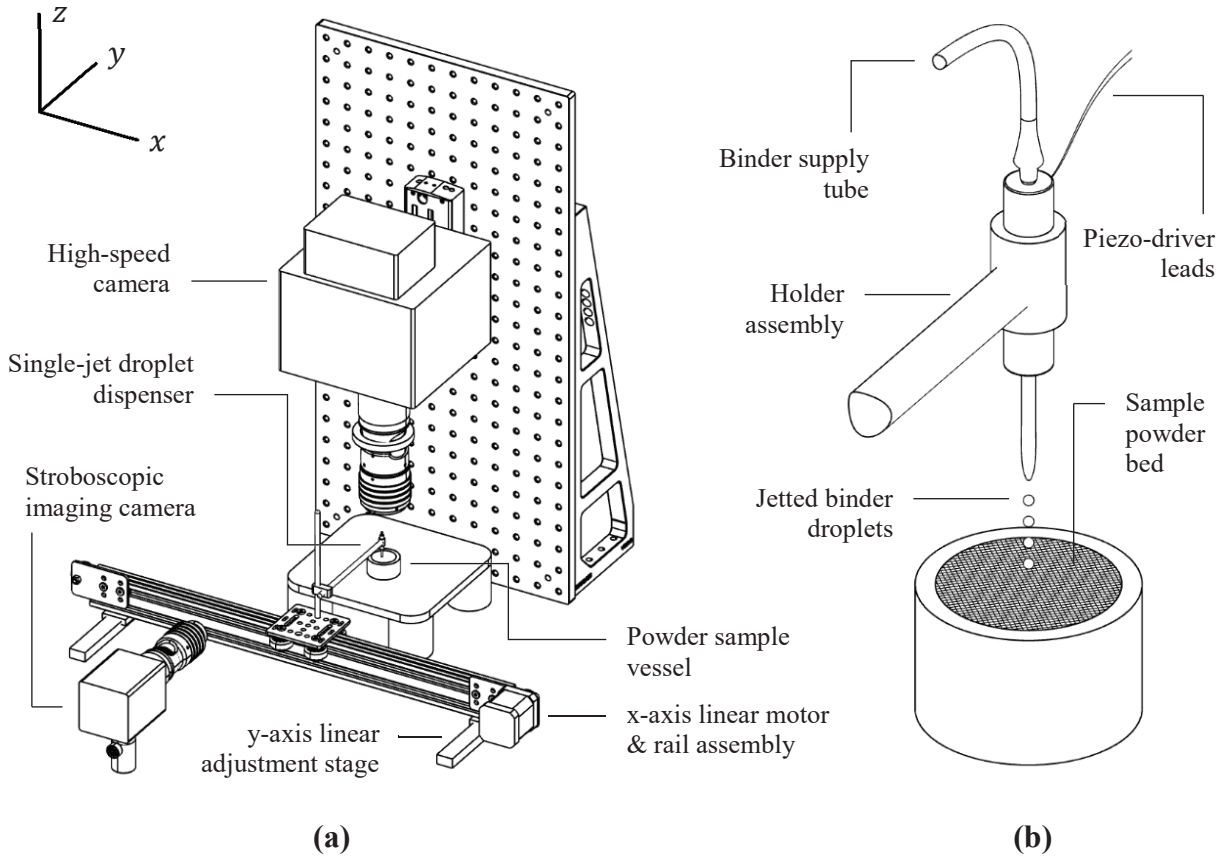


**FIGURE 2.** Experimental apparatus for investigating single-line primitive formation. **(a)** Diagram of the entire setup. **(b)** Magnified diagram of the single-jet droplet dispenser and powder sample.

frequency, $f_j$, and droplet speed, $U_j$, along the jet trajectory. The 53 μm orifice on the dispenser nozzle produces droplet sizes on the order of 50 μm. The droplet diameter can be slightly adjusted by varying the parameters of piezoelectric actuation.

The powder sample is contained in a cylindrical vessel having a diameter and height of 1 cm. In this work, the fundamental phenomenon of line primitive formation on the surface of an unbound powder bed is considered; therefore, a thin layer thickness is not currently imposed. After the powder is loaded, the vessel is lightly tapped and the powder bed surface is smoothed by manually spreading the excess powder with a lab spatula. Future work will examine the effect of layer thickness on the line primitive and will replicate the BJ3DP spreading process to greater fidelity. Highly spherical, plasma atomized Inconel 718 powder is used. The particle diameter range is 20-38 μm and the tapped packing fraction $\phi$ is approximately 0.53. Inconel is a nickel-chromium-based superalloy that maintains high strength at extreme temperatures and has excellent oxidation and corrosion resistance [26]. For these reasons, Inconel alloy components are commonly used in gas-turbine engines, combustion chambers, nuclear reactors, and other demanding applications involving high thermal loading. Currently, BJ3DP has been employed to manufacture components from Inconel 625 and Inconel 718 powder feedstocks [27, 28]; however,

further work is required to mitigate part defects introduced by the process before the components can be used in mission-critical and high-performance applications.

A Vision Research Phantom VEO high-speed camera with a 4.5X microscope objective is mounted above the powder sample and droplet dispenser assembly. Various camera angles were attempted such that the line of sight of the camera intersected the powder bed at an oblique angle rather than perpendicular to it; however, because of the shallow depth of field at high magnification, a purely top-down arrangement with the camera's line of sight parallel to the z-axis (as it is in Fig. 2a) produced the best results. In this configuration, view of the droplet impact location on the powder bed is obstructed by the single-jet dispenser (Fig. 3a). This issue is addressed by positioning the dispenser with a slight angle $\beta$ about the y-axis in order to move the droplet impact location in the line of sight of the camera (Fig. 3b). Assuming the translational dispenser motion is from right to left in Fig. 3 and negating aerodynamic drag, the x- and z-components of the droplet impact velocity can be approximated by

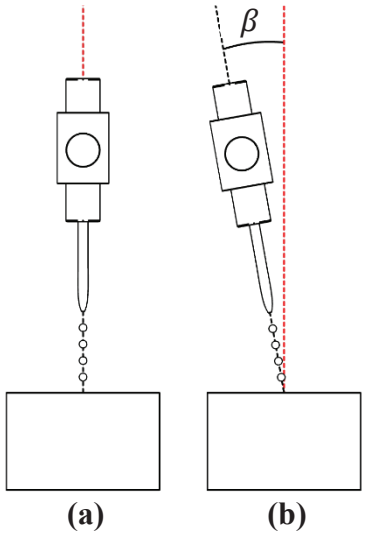


**FIGURE 3.** Configuration of the dispensing device. The red dashed line is the camera line of sight, and the black dashed line is the straight line jet trajectory.

$$u_x = U_d - U_j \sin\beta\,, \quad u_z = U_j \cos\beta\,. \tag{3}$$

This jetting speed is obtained using stroboscopic imaging with a charge-coupled device (CCD) camera and a mounted light-emitting diode (LED) strobe. The basic operation of synchronized stroboscopic illumination is shown in Fig. 4. The strobe is illuminated at a frequency that is synchronized with the piezoelectric actuation of the dispenser. A small time delay $\tau$ is imposed between the jet initiation and LED pulses; thus, a low framerate camera (typically 24-60 frames per second) will only capture what appears to be a single stationary droplet at some position along its trajectory [30]. The distance of the "pseudo-stationary" droplet from the dispenser orifice, $d_{ps}$, and the time delay can be used to calculate the jetting velocity as $U_j = d_{ps}/\tau$. Furthermore, the droplet diameter is also easily obtained from the stroboscopic images. Consequently, this method allows for measurements of the jetting parameters without the need for an additional high-speed camera.

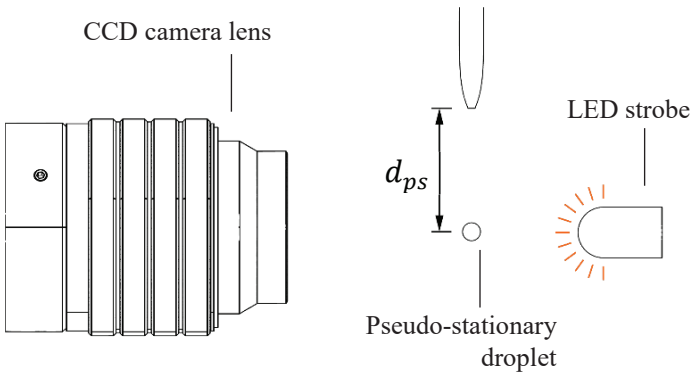


**FIGURE 4.** A general stroboscopic imaging setup.

For obtaining quantitative data of the resulting line primitive, a common digital single-lens reflex (DSLR) camera with a microscope objective attachment can be installed

in place of the high-speed camera. Still frame images are taken from above shortly after the conclusion of a single-line print operation. Due to the small volume of binder jetted (~50 picoliters per drop), it can be difficult to discern the liquid within the bed, even when high magnification is used. This issue is made less severe by introducing a small amount of fluorescent dye to the binder prior to jetting. This causes the liquid contained within the line primitives to illuminate upon exposure to ultraviolet light.

## 4. DIMENSIONAL ANALYSIS

A dimensional analysis is carried out to aid in the design of experiments of single-line primitive formation. Dimensional analysis is a powerful technique that can reduce the number of independent variables in the problem by grouping them into a fundamental set of nondimensional parameters for which the problem depends [31]. To do this, all parameters that can affect the fluid-particle interaction in a single-line print must be considered. The problem being analyzed is that of a continuous droplet train impacting a powder bed. The droplets are generated from a single-jet dispensing device translating over a powder bed at a constant speed. Each droplet is assumed to be spherical and of fixed diameter – satellite droplets are not currently considered. Additionally, temperature is assumed to only affect the material properties of the binder and powder. Although their influence may be significant, evaporation and other phase change effects are not considered here. Finally, the dispenser angle $\beta$ is set to zero; therefore, $u_x = U_d$ and $u_z = U_j$. Given the problem statement and the aforementioned assumptions, the relevant parameters and their nomenclature are given in Table 1.

**TABLE 1.** Nomenclature and important parameters in a single-line primitive formation event. The fundamental dimensions comprising each parameter are mass (M), length (L), and time (T). Hyphens indicate dimensionless values.

| Symbol | Description | Dimensions |
|---|---|---|
| *Process Parameters* | | |
| $f_j$ | Jetting frequency | $T^{-1}$ |
| $u_x$ | x-component of impact velocity | $LT^{-1}$ |
| $u_z$ | z-component of impact velocity | $LT^{-1}$ |
| $D_b$ | Binder droplet diameter | L |
| *Fluid Properties* | | |
| $\rho_b$ | Binder density | $ML^{-3}$ |
| $\mu_b$ | Binder dynamic viscosity | $ML^{-1}T^{-1}$ |
| $\sigma$ | Binder-air surface tension coefficient | $MT^{-2}$ |
| *Particle Properties* | | |
| $\rho_p$ | Particle (powder) density | $ML^{-3}$ |
| $D_p$ | Particle diameter | L |
| $\phi$ | Packing fraction | - |
| $c$ | Cohesion | $ML^{-1}T^{-2}$ |
| $\alpha_f$ | Angle of internal friction | - |
| *System Properties* | | |
| $\theta_c$ | Binder-particle-air contact angle | - |
| $g$ | Gravitational acceleration | $LT^{-2}$ |

If it is assumed that some response variable $R$ exists that serves as a measure of the quality of the line primitive, a functional relationship between the response and independent parameters is in the form

$$R = f\left(f_j, u_x, u_z, D_b, \rho_b, \mu_b, \sigma, \rho_p, D_p, \phi, c, \alpha_f, \theta_c, g\right). \quad (5)$$

The determination of what measures should be used for $R$ to provide adequate quantification of the primitive line quality is not obvious. In this study, two response variables are considered: 1) the fractional area coverage, $AF$, of a line primitive contour with its bounding box, and 2) the bounding box width $w$. As shown in Fig. 5, the red bounding box is constructed from the four extreme points (top, bottom, left, and right) of the 2D primitive line contour. The area fraction is calculated by $AF = A_{lp}/(l \cdot w)$, where $A_{lp}$ is the gray region representing the bound line primitive in Fig. 5. It is clear from Eq. (5) that $R$ is some function of the fourteen independent parameters given in Table 1. With Buckingham's Pi theorem, Eq. (5) is cast into another functional relationship between the nondimensional groups that can be constructed from all of the independent and dependent variables:

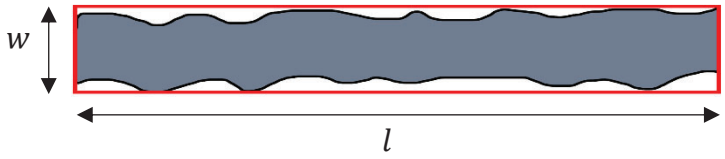


**FIGURE 5.** Line primitive shape (gray) and bounding box (red).

**TABLE 2.** Π –terms obtained by dimensional analysis and appropriate classical names.

| Π -term | ND group | Classical name |
|---|---|---|
| $\Pi_1$ | $AF$ or $w/D_b$ | - |
| $\Pi_2$ | $\rho_b u_z D_b/\mu_b$ | Reynolds No. ($Re$) |
| $\Pi_3$ | $\rho_b D_b u_z^2/\sigma$ | Weber No. ($We$) |
| $\Pi_4$ | $\rho_b/\rho_p$ | - |
| $\Pi_5$ | $D_b/D_p$ | - |
| $\Pi_6$ | $\phi$ | - |
| $\Pi_7$ | $c/\rho_b u_z^2$ | - |
| $\Pi_8$ | $\alpha_f$ | - |
| $\Pi_9$ | $\theta_c$ | - |
| $\Pi_{10}$ | $\rho_b g D_b^2/\sigma$ | Bond No. ($Bo$) |
| $\Pi_{11}$ | $f_j D_b/u_x$ | Strouhal No. ($St$) |
| $\Pi_{12}$ | $u_x/u_z$ | - |

$$\Pi_1 = g(\Pi_2, \Pi_3, \Pi_4, \ldots, \Pi_{12}), \quad (6)$$

where each Π term represents a nondimensional group – these terms are defined in Table 2. The $\Pi_1$ term depends on which response variable is being considered ($R = AF$ or $R = w$). The terms $\Pi_2$-$\Pi_{12}$ are independent of the response variable; however, the function $g$ relating these terms to $\Pi_1$ will differ depending on which $R$ is chosen.

From Table 2, several common nondimensional (ND) groups in fluid mechanics are apparent: $\Pi_2 = Re$ (Reynolds number), $\Pi_3 = We$ (Weber number), $\Pi_{10} = Bo$ (Bond number), and $\Pi_{11} = St$ (Strouhal number). The terms $\Pi_1$, $\Pi_2$, $\Pi_3$, $\Pi_{11}$, and $\Pi_{12}$ are of primary focus in this work since they

are the only ones that contain printing process parameters that can be tuned on an actual 3D printer. We currently assume a cohesionless powder; thus, $\Pi_7$ is disregarded.

## 5. RESULTS

Several single-line printing tests are carried out using both the high-speed and still frame imaging setups on the experimental apparatus. As mentioned in the previous section, only the parameters $\Pi_1, \Pi_2, \Pi_3, \Pi_{11}$, and $\Pi_{12}$ are considered. Since an aqueous binder is used, the fluid properties are taken as that of water – the actual binder properties will be measured in future work. The dispenser is set to jet droplets of $D_b = 54.35$ µm and $u_z = 8.33$ m/s. These values are held constant for all tests, requiring that $Re = 452.74$ and $We = 52.38$ also remain constant as long as the fluid properties are unchanged. When $u_x$ is the only parameter that is adjusted, both $\Pi_{11}$ and $\Pi_{12}$ are affected. The jetting frequency, which only $\Pi_{11}$ is dependent on, can also be varied; however, it is difficult to adjust $f_j$ without inadvertently changing $D_b$ and $u_z$. This issue is presently being addressed and is deferred to later studies.

Still frames extracted from the high-speed videos are shown in Fig. 6. The x-component of the droplet impact velocity for this case is $u_x = 0.127$ m/s. In agreeance with the findings in [29], a significant number of ballistic particle ejections were observed. Furthermore, several tests were performed with a lower vertical impact speed ($u_z = 2.95$ m/s) and particle ejections were still prevalent, albeit with reduced occurrences. For lower vertical impact speeds, the line primitives were found to be more susceptible to breakup. This is attributed to the "balling" phenomenon, which is the result of the Plateau-Rayleigh instability in liquid filaments [32]. Balling in BJ3DP was discussed in Refs. [3, 17].

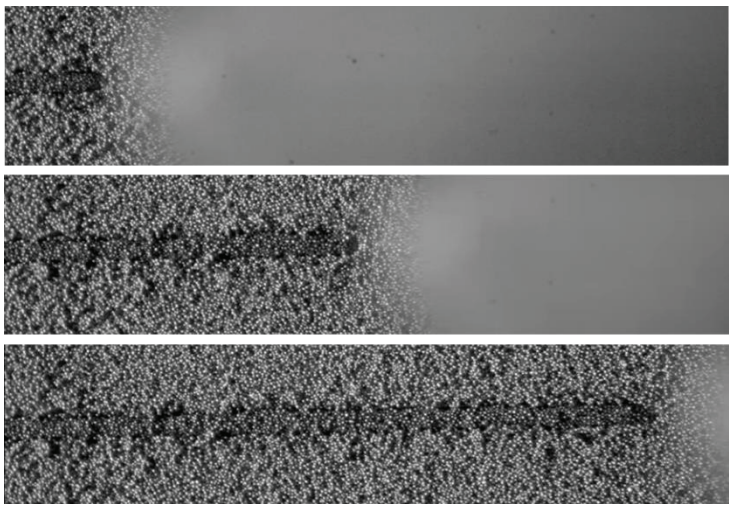

**FIGURE 6.** Still frames captured from high-speed video of the droplet dispenser traversing from left to right. The frames are in downward sequential order.

Four trials are performed utilizing the still frame imaging setup for a $u_x$ range of 0.016-0.127 m/s. The resulting line primitives are shown in Figs. 7-10 in order of decreasing $\Pi_{11}$ ($St$) and $\Pi_{12}$ ($u_x/u_z$). The line primitive contours are generated using image processing software developed in-house. Due to the illumination of the fluorescent binder, the line primitive edges are clearly delineated. The line primitive shape and bounding box for each trial is given in Fig. 11. Unsurprisingly, from Figs. 7-11, it is evident that the bounding box width increases as $\Pi_{11}$ is decreased. This is attributed to the fact that $\Pi_{11}$ is the inverse of the ratio of droplet spacing (Eq. 2) to droplet diameter; thus, a lower value indicates a larger volume of binder being deposited during the dispenser translation. In addition to the width increase, $AF$ also increases with decreasing $\Pi_{11}$. The results for the four trials are given in Table 3.

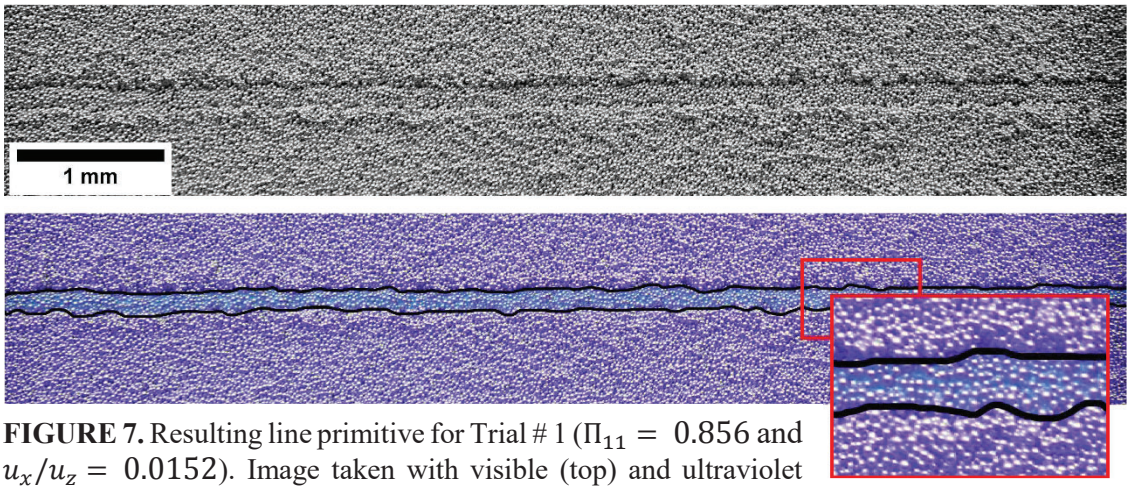


**FIGURE 7.** Resulting line primitive for Trial # 1 ($\Pi_{11} = 0.856$ and $u_x/u_z = 0.0152$). Image taken with visible (top) and ultraviolet (bottom) light.

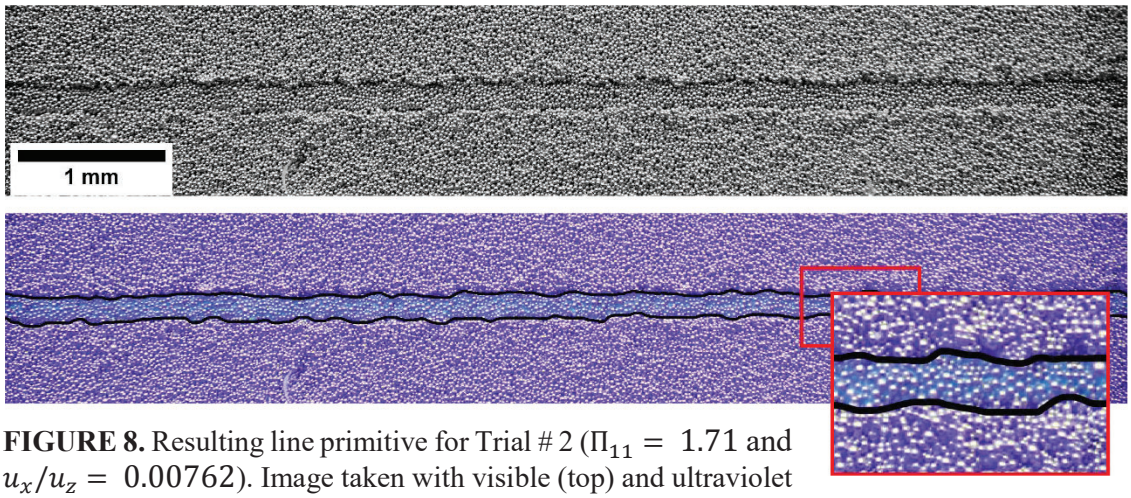


**FIGURE 8.** Resulting line primitive for Trial # 2 ($\Pi_{11} = 1.71$ and $u_x/u_z = 0.00762$). Image taken with visible (top) and ultraviolet (bottom) light.

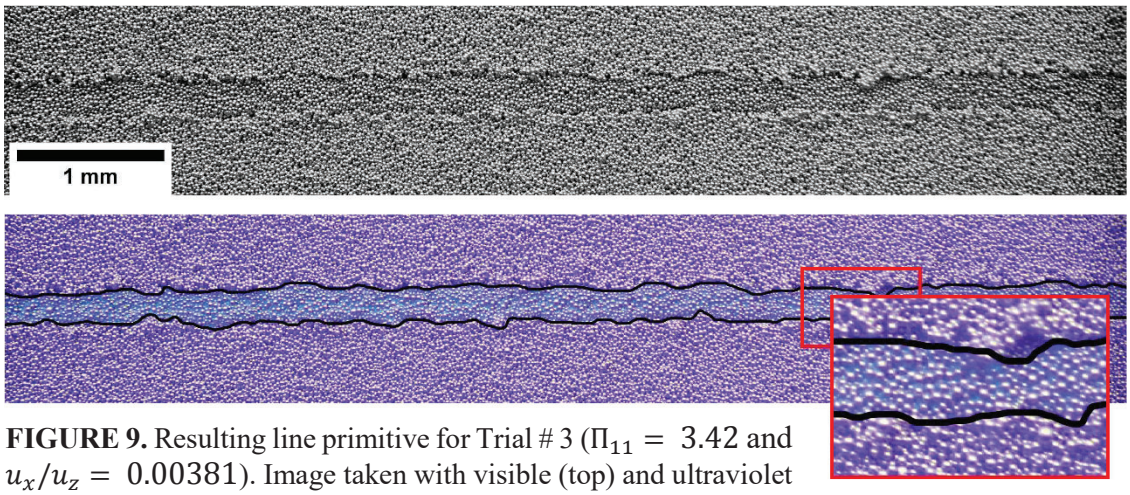


**FIGURE 9.** Resulting line primitive for Trial # 3 ($\Pi_{11} = 3.42$ and $u_x/u_z = 0.00381$). Image taken with visible (top) and ultraviolet (bottom) light.

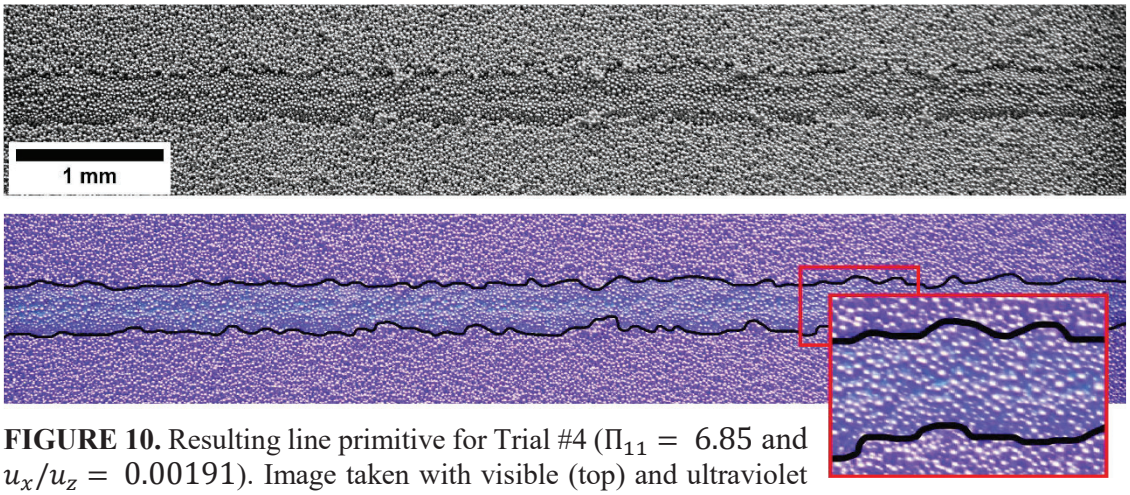


**FIGURE 10.** Resulting line primitive for Trial #4 ($\Pi_{11} = 6.85$ and $u_x/u_z = 0.00191$). Image taken with visible (top) and ultraviolet (bottom) light.

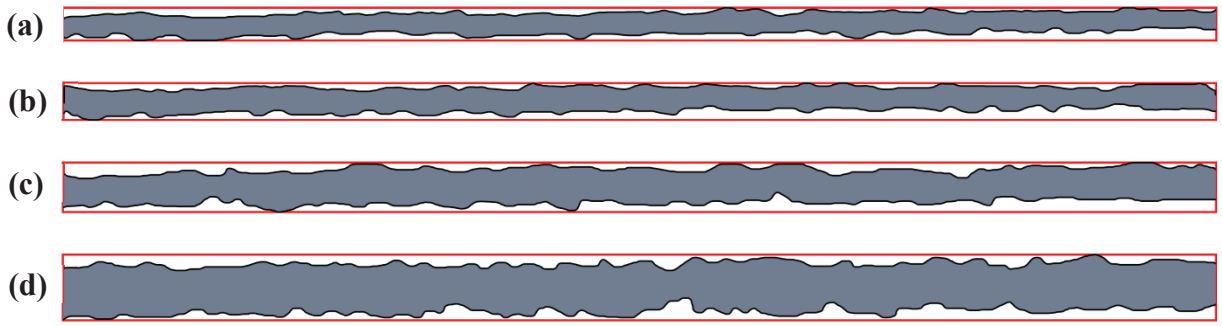


**FIGURE 11.** Line primitive shapes and corresponding bounding boxes for Trials #1 **(a)**, #2 **(b)**, #3 **(c)**, and #4 **(d)**.

**TABLE 3.** Input ($\Pi_{11}$ and $u_x/u_z$) and output parameters ($AF$ and $w/D_b$) for all trials.

| Trial # | $\Pi_{11}$ $(St)$ | $u_x/u_z$ | $AF$ | $w/D_b$ |
|---|---|---|---|---|
| 1 | 0.856 | 0.0152 | 0.642 | 4.45 |
| 2 | 1.71 | 0.00762 | 0.654 | 5.01 |
| 3 | 3.42 | 0.00381 | 0.673 | 6.59 |
| 4 | 6.85 | 0.00191 | 0.731 | 8.65 |

## 6. CONCLUSION

An experimental apparatus and procedure have been presented to investigate the fluid-particle interaction occurring in the fundamental operation of binder jet 3D printing, namely the binding of a single-line primitive feature. The characteristics of the line primitives that make up the part largely influence its mechanical properties, dimensional accuracy, resolution, and overall quality. This work will aid in the improvement of such attributes by providing an experimental platform to investigate the relationship between the binding process parameters and the resulting

line primitives. With this insight, an optimal combination of process parameters that yield the highest quality components may be discovered for any powder feedstock.

In this study, the apparatus was employed to investigate single-line primitive formation on Inconel powder at various translational dispenser speeds. The area fraction and width of the line primitives were both shown to increase with decreasing translational speed. In future work, the test platform described here will be employed to perform extensive parametric studies on line primitive formation for various powder samples. The final parts will then be examined to reveal whether superior mechanical properties and performance characteristics have been achieved by intelligently tuning the printing parameters. Additionally, the apparatus will serve as an invaluable validation suite for high-fidelity models that attempt to simulate the process.

## ACKNOWLEDGEMENTS

The authors would like to thank The ExOne Company and MicroFab, Inc. for their help and in-kind support during this work. The authors would also like to thank Advanced Powders & Coatings, Inc, (A GE Company) for donating powder samples used in early stages of the project.

## REFERENCES

[1] E. Sachs, M. Cima, P. Williams, D. Brancazio and J. Cornie, "Three Dimensional Printing: Rapid Tooling and Prototypes Directly from a CAD Model," *Journal of Engineering for Industry,* vol. 114, pp. 481-488, 1992.

[2] W. Gao, Y. Zhang, D. Ramanujan, K. Ramani, Y. Chen, C. B. Williams, C. C. L. Wang, Y. C. Shin, S. Zhang and P. D. Zavattieri, "The status, challenges, and future of additive manufacturing in engineering," *Computer-Aided Design,* vol. 69, pp. 65-89, 2015.

[3] M. Ziaee and N. B. Crane, "Binder jetting: A review of process, materials, and methods," *Additive Manufacturing,* vol. 28, pp. 781-801, 2019.

[4] P. K. Gokuldoss, S. Kolla and J. Eckert, "Additive Manufacturing Processes: Selective Laser Melting, Electron Beam Melting, and Binder Jetting - Selection Guidelines," *Materials,* vol. 10, no. 6, 2017.

[5] P. R. Gradl, S. E. Greene and C. S. Protz, "Development and Hot-fire Testing of Additively Manufactured Copper Combustion Chambers for Liquid Rocket Engine Applications," in *53rd AIAA/SAE/ASEE Joint Propulsion Conference*, Atlanta, GA, 2017.

[6] Y. Zhong, L.-E. Ranner, L. Liu, A. Koptyug, S. Wikman, J. Olsen, D. Cui and Z. Shen, "Additive manufacturing of 316L stainless steel by electron beam melting for nuclear fusion applications," *Journal of Nuclear Materials,* vol. 486, pp. 234-245, 2017.

[7] S. Yang and J. R. Evans, "Metering and dispensing of powder; the quest for new solid freeforming techniques," *Powder Technology,* vol. 178, pp. 56-72, 2007.

[8] W. Nan, M. Pasha, T. Bonakdar, A. Lopez, U. Zafar, S. Nadimi and M. Ghadiri, "Jamming during particle spreading in additive manufacturing," *Powder Technology,* vol. 338, pp. 253-262, 2018.

[9] W. Zhang, A. Mehta, P. Desai and C. F. Higgs III, "Machine learning enabled powder spreading process map for metal additive manufacturing (AM)," in *Proceedings of the 28th Annual International Solid Freeform Fabrication Symposium*, Austin, TX, 2017.

[10] N. B. Crane, J. Wilkes, E. Sachs and S. M. Allen, "Improving accuracy of powder sintering-based SFF processes by metal deposition from nanoparticle dispersion," in *Proceedings of the 15th Annual International Solid Freeform Fabrication Symposium*, Austin. TX, 2005.

[11] Y. Bai and C. B. Williams, "Binder jetting additive manufacturing with a particle-free metal ink as a binder precursor," *Materials & Design,* vol. 147, pp. 146-156, 2018.

[12] L. O. Grant, M. B. Alameen, R. Carazzone, C. F. Higgs III and Z. C. Cordero, "Mitigating distortion during sintering of binder jet printed ceramics," in *Proceedings of the 29th Annual International Solid Freeform Fabrication Symposium*, Austin, TX, 2018.

[13] T. Fan, "Droplet-powder impact interaction in three dimensional printing," Ph.D. dissertation, Dept. of Mech. Eng., MIT, Cambridge, MA, 1996.

[14] J. Bredt, "Binder stability and powder-binder interaction in three-dimensional printing," Ph.D. dissertation, Dept. of Mech. Eng., MIT, Cambridge, MA, 1995.

[15] E. Sachs, M. Cima, J. Cornie, D. Brancazio, J. Bredt, A. Curodeau, T. Fan, S. Khanuja, A. Lauder, J. Lee and S. Michaels, "Three-Dimensional Printing: The Physics and Implications of Additive Manufacturing," *CIRP Annals - Manufacturing Technology,* vol. 42, no. 1, pp. 257-260, 1993.

[16] P. Baker, "Three dimensional printing with fine metal powders," Ph.D. dissertation, Dept. of Mech. Eng., MIT, Cambridge, MA, 1995.

[17] K. J. Seluga, "Three Dimensional Printing by Vector Printing of Fine Metal Powders," Ph.D. dissertation, Dept. of Mech. Eng., MIT, Cambridge, MA, 2001.

[18] H. Miyanaji, S. Zhang and L. Yang, "A new physics-based model for equilibrium saturation determination in binder jetting additive manufacturing process," *International Journal of Machine Tools and Manufacture,* vol. 124, pp. 1-11, 2018.

[19] J. Bear, Dynamics of Fluids in Porous Media, New York, NY: American Elsevier Publishing Company, 1972.

[20] H. Chen and Y. F. Zhao, "Process parameters optimization forimproving surface quality and manufacturingaccuracy of binder jetting additivemanufacturing process," *Rapid Prototyping Journal,* vol. 22, no. 3, pp. 527-538, 2016.

[21] S. Shrestha and G. Manogharan, "Optimization of Binder Jetting Using Taguchi Method," *JOM,* vol. 69, no. 3, pp. 491-497, 2017.

[22] K. Lu and W. T. Reynolds, "3DP process for fine mesh structure printing," *Powder Technology,* vol. 187, no. 1, pp. 11-18, 2008.

[23] M. Vaezi and C. K. Chua, "Effects of layer thickness and binder saturation level parameters on 3D printing process," *The International Journal of Advanced Manufacturing Technology,* vol. 53, no. 1-4, pp. 275-284, 2010.

[24] S. M. Gaytan, M. A. Cadena, H. Karim, D. Delfin, Y. Lin, D. Espalin, E. MacDonald and R. B. Wicker, "Fabrication of barium titanate by binder jetting additive manufacturing technology," *Ceramics International,* vol. 41, no. 5, pp. 6610-6619, 2015.

[25] M. Kafara, J. Kemnitzer, H. H. Westermann and R. Steinhilper, "Influence of Binder Quantity on Dimensional Accuracy and Resilience in 3D-Printing," *Procedia Manufacturing,* vol. 21, pp. 638-646, 2018.

[26] Q. Jia and D. Gu, "Selective laser melting additive manufacturing of Inconel 718 superalloy parts: Densification, microstructure and properties," *Journal of Alloys and Compounds,* vol. 585, pp. 713-721, 2014.

[27] A. Mostafaei, E. L. Stevens, E. T. Hughes, S. D. Biery, C. Hilla and M. Chmielus, "Powder bed binder jet printed alloy 625: Densification, microstructure and mechanical properties," *Materials & Desgin,* vol. 108, pp. 126-135, 2016.

[28] P. Nandwana, A. M. Elliott, D. Siddel, A. Merriman, W. H. Peter and S. B. Babu, "Powder bed binder jet 3D printing of Inconel 718: Densification,microstructural evolution and challenges," *Current Opinion in Solid State and Materials Science,* vol. 21, no. 4, pp. 207-218, 2017.

[29] N. D. Parab, J. E. Barnes, C. Zhao, R. W. Cunningham, K. Fezzaa, A. D. Rollett and T. Sun, "Real time observation of binder jetting printing process using high-speed X-ray imaging," *Scientific Reports,* vol. 9, no. 1, p. 2499, 2019.

[30] "Ink-Jet microdispensing, a basic set-up," MicroFab Technologies, Inc., Plano, TX, 2012.

[31] Y. A. Cengel and J. M. Cimbala, Fluid Mechanics: Fundementals and Applications, New York, NY: Mcgraw-Hill, 2006.

[32] L. Rayleigh, "On the instability of jets," *Proceedings of the London mathematical society,* vol. 1, no. 1, pp. 4-13, 1878.